Dalton Transactions

Luminescent Hybrid Halides with Various Centering Metal Cations (Zn, Cd and Pb) and Diverse Structures

Journal:	*Dalton Transactions*
Manuscript ID	DT-ART-12-2022-004067.R1
Article Type:	Paper
Date Submitted by the Author:	04-Mar-2023

Complete List of Authors:	Fan, Liubing; University of Science and Technology Beijing Hao, Shiqiang; Northwestern University, Materials Science He, Shihui; University of Science and Technology Beijing Zhang, Xusheng; University of Science and Technology Beijing Li, Mingyang; University of Science and Technology Beijing School of Materials Science and Engineering Wolverton, Chris; Northwestern University, Department of Materials Science and Engineering Zhao, Jing; University of Science and Technology Beijing, School of Materials Science and Engineering Liu, Quanlin; University of Science and Technology Beijing, School of Materials science & engineering

ARTICLE

Luminescent Hybrid Halides with Various Centering Metal Cations (Zn, Cd and Pb) and Diverse Structures

Received 00th January 20xx,
Accepted 00th January 20xx

DOI: 10.1039/x0xx00000x

Liubing Fan,[a] Shiqiang Hao,[b] Shihui He,[a] Xusheng Zhang,[a] Mingyang Li,[a] Christopher Wolverton,[b] Jing Zhao*[a] and Quanlin Liu[a]

Organic–inorganic hybrid metal halides have been extensively studied because of their great potential in optoelectronics. Herein, we report three hybrid metal halides $(Bmpip)_2ZnBr_4$, $(Bmpip)_2CdBr_4$, and $(Bmpip)_8Pb_{11}Br_{30}$ (where $Bmpip^+$ is 1-butyl-1methyl-piperidinium, $C_{10}H_{22}N^+$). $(Bmpip)_2ZnBr_4$ and $(Bmpip)_2CdBr_4$ crystallize in the $P2_1/c$ space group with zero-dimensional crystal structures with $[MBr_4]^{2-}$ (M = Zn, Cd) tetrahedra isolated by $Bmpip^+$. $(Bmpip)_8Pb_{11}Br_{30}$ crystallizes in the triclinic space group P-1 with one-dimensional corrugated chains constructed by face-sharing $[PbBr_6]^{4-}$ octahedra. All the compounds exhibit excellent ambient and thermal stability. Under UV excitation, all three compounds exhibit very broad emission. Temperature-dependent photoluminescence measurements indicate that the broad emissions of $(Bmpip)_2ZnBr_4$ and $(Bmpip)_2CdBr_4$ can be attributed to both the organic cations and self-trapped excitons (STEs) and that the emission of $(Bmpip)_8Pb_{11}Br_{30}$ is assigned to STEs. Density functional theory calculations reveal that the three compounds all adopt a direct bandgap. This work enriches our understanding of the structure type of hybrid metal halides while unveiling the diverse emission mechanisms.

1. Introduction

Organic–inorganic hybrid metal halides with rich structural and optical properties are emerging as a new class of optoelectronic materials.[1, 2] Lead-based hybrid metal halides with three-dimensional (3D) perovskite structures have been intensively studied in the field of solar cells.[3] The 3D hybrid perovskite structure has the general formula of ABX_3, where A represents small organic cations MA^+ or FA^+ (MA = methylammonium, FA = formamidinium).[4] By breaking the 3D lattice using bulky organic cations, the structural dimensions are reduced to two-dimensional (2D), one-dimensional (1D), and zero-dimensional (0D) structures.[5, 6] Low-dimensional hybrid metal halides exhibit interesting efficient broadband emission originating from self-trapped excitons (STEs) due to stronger electron–phonon coupling.[7]

2D Pb-based hybrid halides have been widely investigated, and their structure (including different layer thicknesses and orientations) can be controlled by adjusting several factors.[8] The first broadband white-light emitter was also discovered in the 2D hybrid halide (N-MEDA)[$PbBr_4$] (N-MEDA = N^1-methylethane-1,2-diammonium).[9] 0D Pb-based hybrid metal halides have been studied for photoluminescence owing to their larger exciton bonding energy and softer lattice, which facilitate STE emission. Six-coordinated octahedron and four-coordinated seesaw lead-based 0D materials have been reported, including $(C_3N_3H_{11}O)_2PbBr_6{\cdot}4H_2O$ and $Bmpip_2PbBr_4$ (Bmpip = 1-butyl-1-methyl-piperidinium).[10, 11] In addition, lead cations can also form clusters, giving them unique properties. Yangui et al. synthesized $(DETA)PbCl_5{\cdot}H_2O$ (DETA = diethylenetriammonium), which exhibits bluish white-light emission with $[Pb_2Cl_{10}]^{6-}$ bioctahedral dimers.[12] Xia and coworkers successfully synthesized $(C_9NH_{20})_9[Pb_3X_{11}](MX_4)_2$ (X = Br and Cl, M = Mn, Fe, Co, Ni, Cu, and Zn) with multiple photoluminescence (PL) centers forming $[Pb_3X_{11}]^{5-}$ trimers.[13, 14] Nowadays, many 1D Pb-based hybrid metal halides have been explored in different field with various structures.[15] Corner- and edge-sharing polyhedrons adopting 1D chain structures have been studied.[16] Although face-sharing 1D structures have not been reported, Kamminga et al. obtained corner-sharing $(C_6H_5CH_2NH_3)_2PbI_4$ and edge-sharing $(C_6H_5CH_2NH_3)_4Pb_5I_{14}{\cdot}2H_2O$.[17]

Recently, d^{10} metal-based hybrid halides have been reported to exhibit excellent PL properties and high stability;[18-20] e.g., $(2cepiH)CdCl_3$ (2cepi = 1-(2-chloroethyl)piperidine) showed broadband white-light emission with a 1D face-sharing $CdCl_6$ structure.[21] Yangui et al. achieved highly efficient (14.87% and 19.18%) white-light emission in $(C_5H_7N_2)_2MBr_4$ (M = Hg, Zn) with a high color rendering index (87 and 96).[22] Hao et al. monitored the red emission with high photoluminescence quantum yield (PLQY) (77.1%) in Zn^{2+}-doped $CsMnCl_3$ nanocrystals.[23] In $BAPPZn_2(Cl_yBr_{1-y})_8$ (BAPP = 1,4-bis(3-ammoniopropyl)piperazinium, y = 0–1), the inorganic host improved the PLQY (24%) and room-temperature phosphorescence properties, which originate from the organic

[a] The Beijing Municipal Key Laboratory of New Energy Materials and Technologies, School of Materials Sciences and Engineering, University of Science and Technology Beijing, Beijing 100083, China.
[b] Department of Materials Science and Engineering, Northwestern University, Evanston, Illinois 60208, United States. E-mail: jingzhao@ustb.edu.cn.
†Electronic Supplementary Information (ESI) available: See DOI: 10.1039/x0xx00000x

molecular structure.[24] In summary, d^{10} cation-based hybrid halides are promising PL materials, and it is urgent to fully characterize their structures and optical properties and explore their applications.

In this work, we report three hybrid metal halides (Bmpip)-*M*–Br (*M* = Zn, Cd and Pb) with dual-band emission, resulting from the organic molecules and STEs. $(Bmpip)_2ZnBr_4$ and $(Bmpip)_2CdBr_4$ adopt 0D crystal structures in the space group $P2_1/c$ with isolated $[MBr_4]^{2-}$ tetrahedra. $(Bmpip)_8Pb_{11}Br_{30}$ crystallizes in space group *P*-1 with a unique face-sharing 1D chain structure. All the compounds exhibit thermal and ambient stability. In addition, under UV light excitation at low temperature, all three compounds exhibit dual-band emission and different colors with increasing temperature. The crystal structures, optical properties, and PL mechanisms are discussed in detail. Our work enriches our understanding of the material system of 1D Pb-based and d^{10} cation-based hybrid metal halides.

2. Experimental Section

2.1 Materials

(Bmpip)Br (97%), $ZnBr_2$ (98%), and $PbBr_2$ (99%) were purchased from Shanghai Aladdin Biochemical Technology Co. and used without further purification. $CdBr_2$ (98%) and hydrobromic acid (HBr, 48 wt.% in water) were purchased from Shanghai Macklin Biochemical Co., Ltd. and used as received.

2.2 Crystal Synthesis

$(Bmpip)_2ZnBr_4$ crystal was synthesized using the slow evaporation method. A mixture of 1.218 g (Bmpip)Br and 0.582 g $ZnBr_2$ with 1 mL of HBr was heated at 55 °C with continuous stirring until a clear solution was obtained. This clear solution was stored at room temperature (RT) for one week and slowly evaporated to obtain white transparent flake crystals of $(Bmpip)_2ZnBr_4$. $(Bmpip)_2CdBr_4$ and $(Bmpip)_8Pb_{11}Br_{30}$ crystals were synthesized using the solution method. A mixture of 0.96 g (Bmpip)Br and 0.44 g $CdBr_2$ was dissolved in 0.5 mL of HBr with stirring at 95 °C, and a clear solution was obtained after slowly cooling to RT. Light yellow crystals of $(Bmpip)_2CdBr_4$ were obtained. A mixture of 0.674 g (Bmpip)Br and 0.526 g $PbBr_2$ was dissolved in 1 mL of HBr under heating at 95 °C with continuous stirring to obtain a clear solution; upon slowly cooling to RT, a milky white block crystal of $(Bmpip)_8Pb_{11}Br_{30}$ was obtained.

2.3 Characterization

Single-crystal X-ray diffraction (SCXRD) data were collected on a Bruker APEX-II CCD diffractometer with a Mo Kα source. All the structures were solved using SHELXS software, and the structural details are provided in the Supporting Information (Table S1–S11).[25] Powder X-ray diffraction (PXRD) analysis was performed on a Bruker D8 Advance powder diffractometer with a Cu Kα radiation source at an operating voltage of 45 kV and current of 40 mA. Thermogravimetric analysis (TGA) and simultaneous differential scanning calorimetry (DSC) were performed on a Setaram Labsys Evo under flowing nitrogen at a heating rate of ±10°C/min. Optical reflection spectra were measured using a SHIMADZU UV-3600, and the absorption spectra were obtained using the Kubelka–Munk equation. Scanning electron microscopy (SEM) imaging and energy-dispersive X-ray spectroscopy (EDS) elemental mapping were performed on a JEOL JSM-6510. RT PL and photoluminescence excitation (PLE) were measured on an Edinburgh FLS920 fluorescence spectrophotometer using a 150 W Xe900 lamp with a PMT detector. The temperature-dependent PL was performed on an Oxford Instruments device cooled by liquid nitrogen.

2.4 Theory Calculations

Density functional theory (DFT) calculations were performed with periodic boundary conditions and a plane-wave basis set as implemented in the Vienna *ab initio* simulation package.[26] The calculations were converged to approximately 3 meV per cation using a basis set energy cutoff of 500 eV and dense *k*-meshes corresponding to 4000 *k*-points per reciprocal atom in the Brillouin zone.

3. Results and discussion

3.1 Crystal Structure

All the crystallographic data and structural refinements of the three compounds are provided in Table 1. $(Bmpip)_2ZnBr_4$ and $(Bmpip)_2CdBr_4$ formed 0D structures, and they both crystallized in the monoclinic system with $P2_1/c$ space group. Zn and Cd formed $[ZnBr_4]^{2-}$ and $[CdBr_4]^{2-}$ tetrahedra with $(Bmpip)^+$ filling in the space (Fig. 1a, b, and c). The Zn–Br bond lengths of $(Bmpip)_2ZnBr_4$ ranged from 2.399(3) to 2.427(3) Å, which are comparable to the values reported in $(C_5H_7N_2)_2ZnBr_4$ (2.382(6)–2.432(6) Å).[22] $(Bmpip)_2CdBr_4$ consists of two crystallographically different Cd with the Cd–Br bond lengths varying between 2.383(2) and 2.646(6) Å, which is comparable to that in $(DMP)CdBr_4$ (2.542(6)–2.660(8) Å) (DMP = N,N'-dimethylpiperazine).[27] The Cd–Br bond lengths are larger than those of Zn–Br resulting from the larger radius of the four-coordinated Cd^{2+} (0.78 Å vs. 0.60 Å for Zn^{2+}).[28] The tetrahedra distortion can be evaluated using Baur distortion indices (DI):[29]

$$\mathrm{DI}\ (M\text{-}X) = \sum_{i=1}^{4} \frac{|d_i - d_m|}{4d_m}$$

$$\mathrm{DI}\ (X\text{-}M\text{-}X) = \sum_{i=1}^{6} \frac{|a_i - a_m|}{6a_m}$$

Here, d_i stands for the individual distances from the metal cations to the halogen anions; a_i are the individual angles of *X*–*M*–*X*; and d_m and a_m signify the average bond distance and bond angle, respectively. DI(*M*–*X*) and DI(*X*–*M*–*X*) of $(Bmpip)_2ZnBr_4$ are 0.0046 and 0.0198, respectively. In $(Bmpip)_2CdBr_4$, Cd(1) with DI(*M*–*X*) and DI(*X*–*M*–*X*) of 0.0144 and 0.0554 and Cd(2) with values of 0.0030 and 0.0354 are larger than those reported for $(C_6H_9N_2)_2ZnCl_4$ (DI(*M*–*X*) = 0.0018 and DI(*X*–*M*–*X*) = 0.0069), possibly stemming from the larger organic cation $Bmpip^+$.[30] The organic cation $Bmpip^+$ (Fig. 1b), owing a structure of six-membered ring and two branched chains, possesses relatively large volume, which interacts with the inorganic moiety resulting in strongly distorted tetrahedra and soft lattice. The structural features make $(Bmpip)_2ZnBr_4$ and $(Bmpip)_2CdBr_4$

exhibit STE emission with large stokes shifts compared with those reported with smaller structural distortions, such as $[CH_3C_6H_4NH_3]_2ZnBr_4$ and $[N(C_3H_7)_4]_2[ZnBr_4]$ which showed no emission at room temperature.[31-33]

$(Bmpip)_8Pb_{11}Br_{30}$ crystallized in the triclinic system with space group *P*-1. Pb forms a unique 1D $[Pb_{11}Br_{30}]^{8-}$ chain via face-sharing Br atoms with $Bmpip^+$ filling the remaining space (Fig. 1d, e). $(Bmpip)_8Pb_{11}Br_{30}$ has six crystallographic positions (labeled as Pb1, Pb2, Pb3, Pb4, Pb5, and Pb6) (Fig. 1f), of which the bond lengths and bond angles of individual Pb are summarized in Table S10–S11. In the lead-bromide chains, the face-sharing Pb1–Pb6 octahedra form a basic structural unit interconnected into an infinite 1D-long chain, where six $[PbBr_6]$ octahedra are connected to form a ring-like structure (Fig. 1f). This unique corrugated 1D structure is different from previously reported edge-sharing corrugated 1D $C_5H_{16}N_2Pb_2Br_6$ and is a new type of 1D metal halide chain structure.[34] The bond-length and bond-angle distortion of the octahedra were evaluated using the following equations:[35]

$$\Delta d = \frac{1}{6}\sum_{i=1}^{6}\left(\frac{d_i - d_m}{d_m}\right)^2$$

$$\sigma^2 = \frac{1}{11}\sum_{i=1}^{12}(\theta_i - 90)^2$$

where d_i are the six individual Pb–Br bond lengths, d_m is the mean value of the Pb–Br bond distance, and θ_i are the Br–Pb–Br angles. The individual Δd and σ^2 of different $[PbBr_6]$ octahedra and average Δd and σ^2 of the whole structure are summarized in Table S12. The average values of Δd and σ^2 are 19.4×10^{-4} and 106.7 deg.^{2}, respectively. These results indicate that the $[PbBr_6]$ octahedra are highly distorted. The Δd value is comparable to that of the previously reported 2D hybrid halide α-(DMEN)$PbBr_4$ (DMEN = 2-(dimethylamino)ethylamine) (Δd = 17.4×10^{-4}).[36] The bond-angle variance of σ^2 is larger than that of $(C_9NH_{20})_9[ZnBr_4]_2[Pb_3Br_{11}]$ (σ^2 = 67.1 deg.^{2}), which adopts a 0D structure with face-sharing trimer clusters.[37] The large structural distortion origins from the organic cation $Bmpip^+$ and unique face-sharing 1D structure which has stronger $[PbBr_6]$ interaction. Meanwhile, the structural distortion and soft lattice result in the formation of different STE energy levels which generate emissions with larger stokes shift compared with $(C_9NH_{20})_9[ZnBr_4]_2[Pb_3Br_{11}]$.[37]

Table 1. Crystal Data and Structure Refinement for (Bmpip)–*M*–Br (*M* = Zn, Cd, and Pb)

Empirical formula	$(C_{10}NH_{22})_2ZnBr_4$	$(C_{10}NH_{22})_2CdBr_4$	$(C_{10}NH_{22})_8Pb_{11}Br_{30}$
Formula weight	697.58	736.73	5910.42
Temperature	293(2) K	293(2) K	293(2) K
Wavelength	0.71069 Å	1.54184 Å	0.71069 Å
Crystal system	monoclinic	monoclinic	triclinic
Space group	$P2_1/c$	$P2_1/c$	P-1
Unit-cell dimensions	a = 16.3329(5) Å, b = 10.5189(4) Å, c = 16.9147(6) Å, β = 111.10°	a = 17.5329(5) Å, b = 9.9301(2) Å, c = 33.1666(6) Å, β = 102.82°	a = 11.9649(1) Å, α = 74.55° b = 16.4760(2) Å, β = 75.12° c = 19.3923(2) Å, γ = 86.03°
Volume	2711.1 Å^3	5630.5 Å^3	3561.2 Å^3
Z	4	8	1
Density (calculated)	1.709 g/cm^3	1.738 g/cm^3	2.756 g/cm^3
Absorption coefficient	6.810 mm^{-1}	12.957 mm^{-1}	21.400 mm^{-1}
F(000)	1392	2856	2640
ϑ range for data collection	2.327 to 26.406°	5.151 to 62.500°	1.840 to 25.000°
Index ranges	$-20 \le h \le 20$, $-13 \le k \le 13$, $-21 \le l \le 20$	$-19 \le h \le 20$, $-11 \le k \le 11$, $-37 \le l \le 38$	$-14 \le h \le 14$, $-19 \le k \le 19$, $-23 \le l \le 23$
Reflections collected	45764	41042	75958
Independent reflections	5560 [R_{int} = 0.0402]	8804 [R_{int} = 0.1022]	12535 [R_{int} = 0.0602]
Completeness to ϑ = 25.00°	99.9%	97.9%	100%
Refinement method	Full-matrix least-squares on F^2	Full-matrix least-squares on F^2	Full-matrix least-squares on F^2
Data / restraints / parameters	5560 / 0 / 248	8804 / 285 / 480	12535 / 790 / 421
Goodness-of-fit	1.032	1.041	1.030
Final R indices [$> 2\sigma(I)$]	R_{obs} = 0.0217, wR_{obs} = 0.0502	*R_{obs} = 0.0869, wR_{obs} = 0.2365*	R_{obs} = 0.0428, wR_{obs} = 0.0936
R indices [all data]	R_{all} = 0.0281, wR_{all} = 0.0527	*R_{all} = 0.1012, wR_{all} = 0.2526*	R_{all} = 0.0550, wR_{all} = 0.0982
Largest diff. peak and hole	0.352 and -0.416 e·Å^{-3}	1.074 and -1.346 e·Å^{-3}	3.312 and -2.615 e·Å^{-3}

$R = \Sigma||F_o| - |F_c|| / \Sigma|F_o|$, $wR = \{\Sigma[w(|F_o|^2 - |F_c|^2)^2] / \Sigma[w(|F_o|^4)]\}^{1/2}$ and $w = 1/[\sigma^2(F_o^2) + (0.0308P)^2 + 60.1359P]$, where $P = (F_o^2 + 2F_c^2) / 3$.

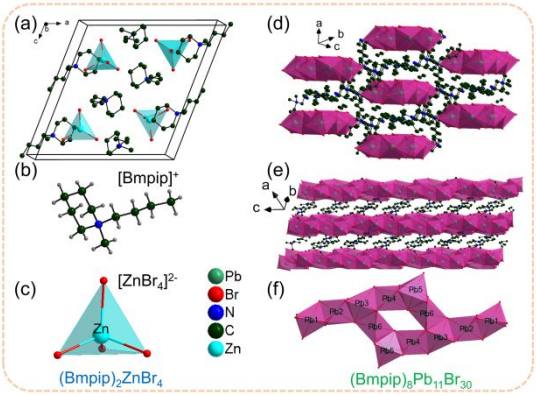

Fig. 1 (a) Crystal structure of $(Bmpip)_2ZnBr_4$. (b) $[Bmpip]^+$ cation. (c) $[ZnBr_4]^{2-}$ tetrahedron. (d) Crystal structure of $(Bmpip)_8Pb_{11}Br_{30}$. (e) Side view of the crystal structure of $(Bmpip)_8Pb_{11}Br_{30}$. (f) Lead-bromide chain.

3.2 Optical properties and stability

Optical and electron microscopy images indicate that the obtained $(Bmpip)_2ZnBr_4$, $(Bmpip)_2CdBr_4$, and $(Bmpip)_8Pb_{11}Br_{30}$ crystals were of high quality (Fig. S1). EDS mapping shows that the elements were homogeneously distributed in the crystals and that the M:Br atomic ratios of $(Bmpip)_2ZnBr_4$, $(Bmpip)_2CdBr_4$, and $(Bmpip)_8Pb_{11}Br_{30}$ are 1:4.5, 1:3.9, and 1:2.9, respectively, which is consistent with the ratios obtained using single-crystal structural refinement (Fig. S1).

The experimental and simulated PXRD patterns of the three compounds are well matched, indicating the high purity of the obtained samples. Furthermore, the PXRD patterns of the three compounds after 8 months of storage in air at RT are in good agreement with those of the freshly synthesized samples, indicating that the three compounds are highly stable in air (Fig. 2a, b, and c). Noteworthy, the experimental PXRD of $(Bmpip)_2ZnBr_4$ has subtle differences with the simulated one. The local details show no additional peaks observed which ensure the phase purity (Fig. S2a). Meanwhile, Rietveld refinement was performed with a χ^2 = 3.98 which can further ensure the phase purity and give accurate cell parameters (Fig. S2b). The cell parameters of powder sample were larger than that obtained by SCXRD (Table S13). The expansion of cell parameters of powder sample compared with single crystal may originate from the process of grinding which introduced defects and disorder. TGA and DSC measurements indicate that all the compounds undergo a two-step decomposition process and are stable up to 283 °C, 291 °C, and 294 °C for $(Bmpip)_2ZnBr_4$, $(Bmpip)_2CdBr_4$, and $(Bmpip)_8Pb_{11}Br_{30}$, respectively. In the first step, the weight loss of $(Bmpip)_2ZnBr_4$, $(Bmpip)_2CdBr_4$, and $(Bmpip)_8Pb_{11}Br_{30}$ was 42%, 63%, and 32%, respectively, which is attributed to the loss of Bmpip (the theoretical values are 45%, 42%, and 21%, respectively) and Br_2.[38] In the DSC curves, two endothermic peaks are observed for the three compounds, which is consistent with the two-step decomposition TGA profile (Fig. 2d, e, and f). Notably, an endothermic peak at 220 °C for $(Bmpip)_8Pb_{11}Br_{30}$ is observed, which indicates a possible phase transition before decomposition.[39] Overall, the three compounds exhibit better thermal stability than that reported for well-known compounds such as $MAPbBr_3$ and $FASnI_3$, which decompose at 176 °C and 100 °C, respectively.[40]

The band gaps were estimated from Tauc plots $[F(R)*h\nu]^2$ to be 5.54, 5.00, and 3.41 eV for $(Bmpip)_2ZnBr_4$, $(Bmpip)_2CdBr_4$, and $(Bmpip)_8Pb_{11}Br_{30}$, respectively (Fig. S3–S5).[34] Band structure calculation based on DFT was performed, and Fig. 3 shows the electronic band structure, indicating that the three compounds all possess a direct bandgap (Fig. S3–S5). Both the conduction band maximum (CBM) and valence band minimum (VBM) are located at the *A*-point, *X*-point, and *Z*-point for $(Bmpip)_2ZnBr_4$, $(Bmpip)_2CdBr_4$, and $(Bmpip)_8Pb_{11}Br_{30}$, respectively. The theoretically calculated band gaps are 4.89, 3.72, and 3.38 eV for $(Bmpip)_2ZnBr_4$, $(Bmpip)_2CdBr_4$, and $(Bmpip)_8Pb_{11}Br_{30}$, respectively. These values are slightly smaller than the experimental values; however, the trend of the theoretical values is consistent with the experimental one. This deviation is common because DFT calculation typically underestimates the band gaps.[41] All three compounds exhibit flat electronic band structures showing highly localized electronic states, resulting from the confined charge carriers.

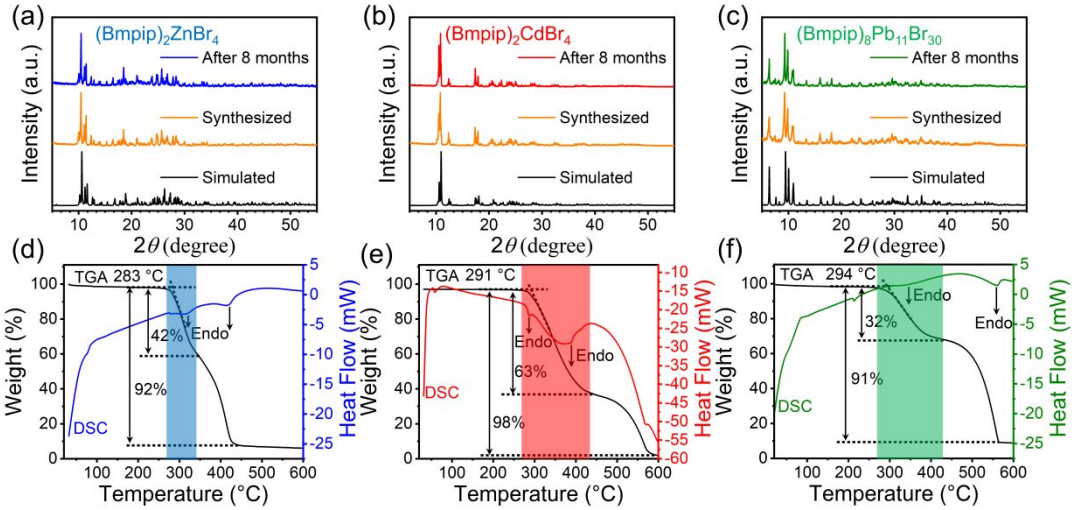

Fig. 2 Comparison of simulated and experimental PXRD patterns of as-synthesized samples and those after storage in air for 8 months at RT for $(Bmpip)_2ZnBr_4$ (a), $(Bmpip)_2CdBr_4$ (b), and $(Bmpip)_8Pb_{11}Br_{30}$ (c). TGA and DSC data for $(Bmpip)_2ZnBr_4$ (d), $(Bmpip)_2CdBr_4$ (e), and $(Bmpip)_8Pb_{11}Br_{30}$ (f).

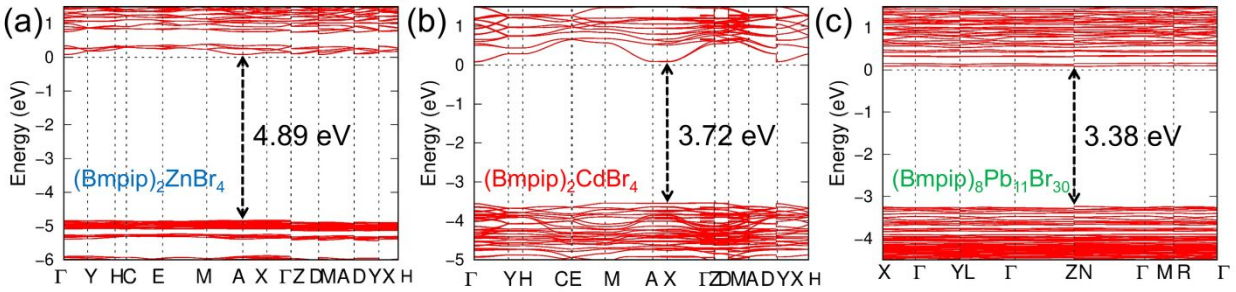

Fig. 3 Electronic band structures of $(Bmpip)_2ZnBr_4$ (a), $(Bmpip)_2CdBr_4$ (b), and $(Bmpip)_8Pb_{11}Br_{30}$ (c).

The PLE spectrum of $(Bmpip)_2ZnBr_4$ has an excitation peak centered at 360 nm, and that of $(Bmpip)_2CdBr_4$ has two excitation peaks at 280 and 316 nm (Fig. 4). Upon 360 nm excitation, $(Bmpip)_2ZnBr_4$ exhibits broadband emission with a maximum intensity of 445 nm and a very broad-tailed peak centered at ~700 nm. Upon 280 nm excitation, $(Bmpip)_2CdBr_4$ shows broad dual-band emission peaks centered at 460 and 730 nm. For comparison, the PLE and PL spectra of the organic salt (Bmpip)Br were measured. (Bmpip)Br exhibits two PLE peaks centered at 257 and 345 nm. Under 257 nm excitation, blue emission centered at 465 nm was observed. Compared with (Bmpip)Br, $(Bmpip)_2ZnBr_4$ and $(Bmpip)_2CdBr_4$ exhibit the same emission peak centered at ~450 nm, indicating that the origin of the 450 nm emission was $Bmpip^+$. $(Bmpip)_8Pb_{11}Br_{30}$ exhibits one excitation peak centered at 382 nm. Under 382 nm excitation, $(Bmpip)_8Pb_{11}Br_{30}$ exhibits emission centered at 530 nm with a Stokes shift of 148 nm and a full width at half-maximum (FWHM) of 0.572 eV. The PL intensity of the three compounds is weak, and the Commission Internationale de l'Eclairage (CIE) chromaticity coordinates are (0.21, 0.19), (0.36, 0.24), and (0.28, 0.54) for $(Bmpip)_2ZnBr_4$, $(Bmpip)_2CdBr_4$, and $(Bmpip)_8Pb_{11}Br_{30}$, respectively (Fig. S6–S8).

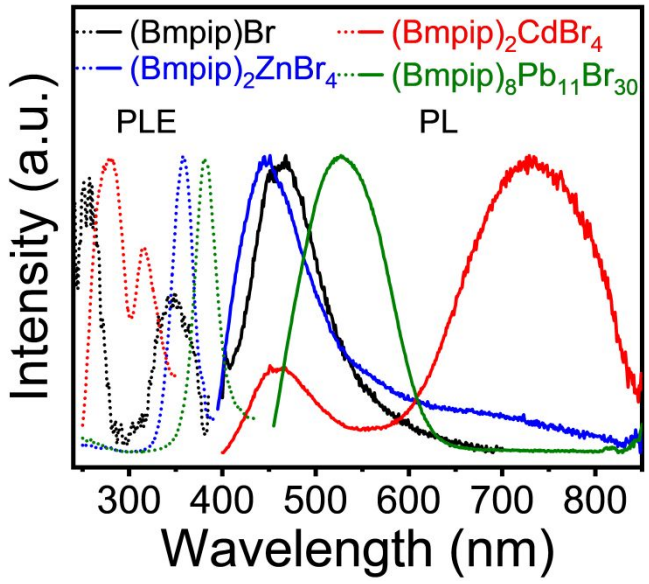

Fig. 4 PLE (dotted line) and PL (solid line) spectra of (Bmpip)Br, $(Bmpip)_2ZnBr_4$, $(Bmpip)_2CdBr_4$, and $(Bmpip)_8Pb_{11}Br_{30}$ at RT.

3.3 Temperature-dependent PL spectra and mechanism

Temperature-dependent PL spectra were obtained to explore the emission mechanism (Fig. 5). For $(Bmpip)_2ZnBr_4$, compared with the RT PL spectrum, significant changes in the relative intensity of the two emission peaks were observed. At 110 K, the intensity of the emission centered at 630 nm was much higher than that at 420 nm. With increasing temperature, the intensity of the two emissions decreased. At 320 K, the 630 nm peak almost disappeared, and the peak of 420 nm was shifted to 445 nm, which matches with the RT PL spectra (Fig. 5a). For $(Bmpip)_2CdBr_4$, the temperature-dependent PL spectra are similar to the RT PL spectra showing dual-band emission at 460 and 725 nm, and the low-temperature PL behavior was similar to that of $(Bmpip)_2ZnBr_4$ (Fig. 5b). For $(Bmpip)_2ZnBr_4$ and $(Bmpip)_2CdBr_4$, the emission peak at ~450 nm is attributed to the organic part, and the low-energy emission is assigned to STEs resulting from the strong electron–phonon coupling (Fig. 5d).[42] The PL properties are similar to those of previously reported compounds. For example, $(C_5H_7N_2)_2ZnBr_4$ achieved broadband white-light emission with the main peak at 535 nm and a shoulder peak at 700 nm, where the high-energy peak results from the organic cation and the low-energy peak originates from the STE emission of $ZnBr_4^{2-}$.[22] $(H_3AEP)_2CdBr_6{\cdot}2Br$ (AEP = 1-(2-aminoethyl)piperazine) exhibits highly efficient orange-red emission with a maximum peak at 612 nm, which originates from STEs.[43]

For $(Bmpip)_8Pb_{11}Br_{30}$, the low-temperature PL spectra differ significantly from the RT PL one with two emission peaks at 465 and 670 nm. At 110 K, the intensities of the two bands are nearly equal. Before 240 K, the 465 nm emission band exhibits anti-thermal quenching behavior. Above 240 K, the intensity of the high-energy emission band begins to decrease. The low-energy emission band continuously decreases with increasing temperature (Fig. 5c). The two emission peaks of $(Bmpip)_8Pb_{11}Br_{30}$ are attributed to different STE emissions similar to $(C_9NH_{20})_9[ZnBr_4]_2[Pb_3Br_{11}]$ and $(C_9NH_{20})_9[ZnCl_4]_2[Pb_3Cl_{11}]$,[37, 44] which display green emission at RT originating from inorganic units and two emission levels at low temperature. In addition, the anti-thermal quenching phenomenon was observed in the two reported compounds mentioned above. The two levels originating from STEs of $(Bmpip)_8Pb_{11}Br_{30}$ were equal under low temperature, and

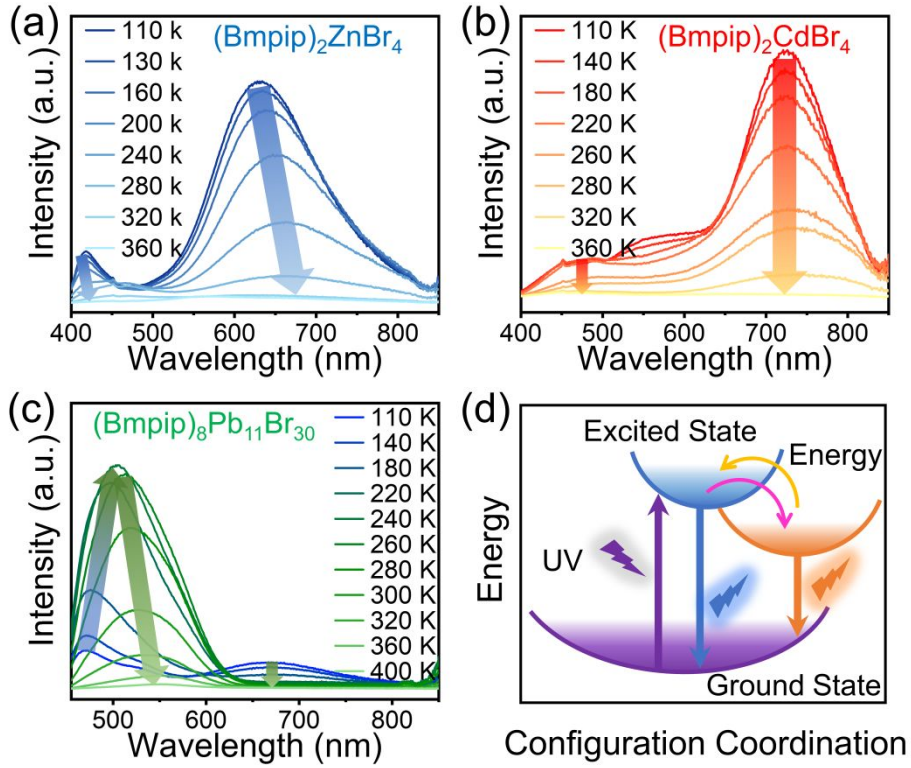

Fig. 5 Temperature-dependent PL spectra of $(Bmpip)_2ZnBr_4$ (a), $(Bmpip)_2CdBr_4$ (b), and $(Bmpip)_8Pb_{11}Br_{30}$ (c). (d) Schematic diagram of emission mechanism for the three compounds.

with increased temperature, the electrons acquired enough energy to jump from a low- to a high-energy level, producing the anti-quenching phenomenon (Fig. 5d). As the temperature changed, the PL color (CIE coordination) of the three compounds changed due to the PL intensity change, indicating the potential for application in temperature detection (Fig. S6–8).

4. Conclusions

Three hybrid metal halides of $(Bmpip)_2ZnBr_4$, $(Bmpip)_2CdBr_4$, and $(Bmpip)_8Pb_{11}Br_{30}$ were synthesized. $(Bmpip)_2ZnBr_4$ and $(Bmpip)_2CdBr_4$ crystallized in the monoclinic space group $P2_1/c$, and $(Bmpip)_8Pb_{11}Br_{30}$ crystallized in the triclinic space group P-1. $(Bmpip)_2ZnBr_4$ and $(Bmpip)_2CdBr_4$ formed a 0D structure with MBr_4^{2-} tetrahedra, and $(Bmpip)_8Pb_{11}Br_{30}$ formed a unique 1D structure with face-sharing octahedra forming chains. All the compounds exhibited good ambient and thermal stability up to 280 °C. Dual-band emission properties were observed at low temperature for the three compounds, which originated from both the organic part and STEs for $(Bmpip)_2ZnBr_4$ and $(Bmpip)_2CdBr_4$ and from the STEs for $(Bmpip)_8Pb_{11}Br_{30}$. Furthermore, the emission color could be tuned by changing the temperature, indicating the potential for application for temperature sensors and detection. The synthesis of the three compounds expands the space of organic–inorganic hybrid metal halides and aids in probing the relationship between their structures and optical properties.

Conflicts of interest

There are no conflicts to declare.

Acknowledgements

This work was supported by the National Natural Science Foundation of China 52272133. This work was also supported by the Fundamental Research Funds for the Central Universities FRF-IDRY-GD21-005. SH and CW are supported by the U.S Department of Energy, Office of Science and Office of Basic Energy Sciences under award number DE-SC0014520.

Notes and references

1. Z. Song, J. Zhao and Q. Liu, Luminescent perovskites: Recent advances in theory and experiments, *Inorga. Chem. Front.*, 2019, **6**, 2969-3011.
2. Y. Dong, Y. Han, R. Chen, Y. Lin and B. Cui, Recent progress of triplet state emission in organic-inorganic hybrid metal halides, *J. Lumin.*, 2022, **249**, 119013.
3. A. Kojima, K. Teshima, Y. Shirai and T. Miyasaka, Organometal halide perovskites as visible-light sensitizers for photovoltaic cells, *J. Am. Chem. Soc.*, 2009, **131**, 6050-6051.
4. L. Mao, P. Guo, M. Kepenekian, I. Spanopoulos, Y. He, C. Katan, J. Even, R. D. Schaller, R. Seshadri, C. C. Stoumpos and M. G. Kanatzidis, Organic cation alloying on intralayer A and

Interlayer A' sites in 2D hybrid dion–jacobson lead bromide perovskites (A')(A)Pb_2Br_7, *J. Am. Chem. Soc.*, 2020, **142**, 8342-8351.
5. C. Zhou, H. Lin, Q. He, L. Xu, M. Worku, M. Chaaban, S. Lee, X. Shi, M. Du and B. Ma, Low dimensional metal halide perovskites and hybrids, *Mat. Sci. Eng. R.*, 2019, **137**, 38-65.
6. L. Xu, H. Lin, S. Lee, C. Zhou, M. Worku, M. Chaaban, Q. He, A. Plaviak, X. Lin, B. Chen, M. Du and B. Ma, 0D and 2D: The cases of phenylethylammonium tin bromide hybrids, *Chem. Mater.*, 2020, **32**, 4692-4698.
7. Y. Ma, Y. Sun, W. Xu, X. Liu, Q. Zhong, Y. Song, H. Fu, C. Yue and X. Lei, Ultrastable 0D organic zinc halides with highly efficient blue light emissions, *Adv. Optical Mater.*, 2022, **10**, 2200386.
8. L. Mao, W. Ke, L. Pedesseau, Y. Wu, C. Katan, J. Even, M. R. Wasielewski, C. C. Stoumpos and M. G. Kanatzidis, Hybrid dion-jacobson 2D lead iodide perovskites, *J. Am. Chem. Soc.*, 2018, **140**, 3775-3783.
9. E. R. Dohner, E. T. Hoke and H. I. Karunadasa, Self-assembly of broadband white-light emitters, *J. Am. Chem. Soc.*, 2014, **136**, 1718-1721.
10. V. Morad, Y. Shynkarenko, S. Yakunin, A. Brumberg, R. D. Schaller and M. V. Kovalenko, Disphenoidal zero-dimensional lead, tin, and germanium halides: Highly emissive singlet and triplet self-trapped excitons and x-ray scintillation, *J. Am. Chem. Soc.*, 2019, **141**, 9764-9768.
11. B. Cui, Y. Han, B. Huang, Y. Zhao, X. Wu, L. Liu, G. Cao, Q. Du, N. Liu, W. Zou, M. Sun, L. Wang, X. Liu, J. Wang, H. Zhou and Q. Chen, Locally collective hydrogen bonding isolates lead octahedra for white emission improvement, *Nat. Commun.*, 2019, **10**, 5190.
12. A. Yangui, R. Roccanova, Y. Wu, M. Du and B. Saparov, Highly efficient broad-band luminescence involving organic and inorganic molecules in a zero-dimensional hybrid lead chloride, *J. Phys. Chem. C*, 2019, **123**, 22470-22477.
13. L. Fan, K. Liu, S. He, F. Zhao, J. Zhao, Y. Wang and Q. Liu, Reversible mechanically induced on-off photoluminescence in hybrid metal halides, *Adv. Funct. Mater.*, 2022, **32**, 2110771.
14. M. Li, M. S. Molokeev, J. Zhao and Z. Xia, Optical functional units in zero‐dimensional metal halides as a paradigm of tunable photoluminescence and multicomponent chromophores, *Adv. Optical Mater.*, 2020, **8**, 1902114.
15. M. Z. Rahaman, S. Ge, C.-H. Lin, Y. Cui and T. Wu, One-dimensional molecular metal halide materials: Structures, properties, and applications, *Small Struct.*, 2021, **2**, 2000062.
16. M. Z. Rahaman, S. Ge, C. Lin, Y. Cui and T. Wu, One‐dimensional molecular metal halide materials: Structures, properties, and applications, *Small Struct.*, 2021, **2**, 2000062.
17. M. E. Kamminga, G. A. de Wijs, R. W. A. Havenith, G. R. Blake and T. T. M. Palstra, The role of connectivity on electronic properties of lead iodide perovskite-derived compounds, *Inorg. Chem.*, 2017, **56**, 8408-8414.
18. R. Msalmi, S. Elleuch, B. Hamdi, W. Abd El-Fattah, N. Ben Hamadi and H. Naïli, Organically tuned white-light emission from two zero-dimensional cd-based hybrids, *RSC Adv.*, 2022, **12**, 10431-10442.
19. T. M. McWhorter, Z. Zhang, T. D. Creason, L. Thomas, M. Du and B. Saparov, $(C_7H_{11}N_2)_2MBr_4$(M = Cu, Zn): X‐ray sensitive 0D hybrid metal halides with tunable broadband emission, *Eur. J. Inorg. Chem.*, 2022, **2022**, e202100954.
20. K. Li, Y. Zhao, M. Sun, G. Chen, C. Zhang, H. Liu, H. Li, S. Zang and T. C. W. Mak, Zero-dimensional zinc halide organic hybrids with excellent optical waveguide properties, *Cryst. Growth & Des.*, 2022, **22**, 3295-3302.
21. Z. Qi, Y. Chen, Y. Guo, X. Yang, F. Zhang, G. Zhou and X. Zhang, Broadband white-light emission in a one-dimensional organic–inorganic hybrid cadmium chloride with face-sharing $CdCl_6$ octahedral chains, *J. Mater. Chem. C*, 2021, **9**, 88-94.
22. A. Yangui, R. Roccanova, T. M. McWhorter, Y. Wu, M. Du and B. Saparov, Hybrid organic–inorganic halides $(C_5H_7N_2)_2MBr_4$ (M = Hg, Zn) with high color rendering index and high-efficiency white-light emission, *Chem. Mater.*, 2019, **31**, 2983-2991.
23. X. Hao, H. Liu, W. Ding, F. Zhang, X. Li and S. Wang, Zn^{2+}-doped lead-free csmncl_3 nanocrystals enable efficient red emission with a high photoluminescence quantum yield, *J. Phys. Chem. Lett.*, 2022, **13**, 4688-4694.
24. J. Wei, W. Ou, J. Luo and D. Kuang, Zero-dimensional zn-based halides with ultra-long room-temperature phosphorescence for time-resolved anti-counterfeiting, *Angew. Chem. Int. Ed. Engl.*, 2022, **61**, e202207985.
25. G. Sheldrick, A short history of shelx, *Acta Crystallogr., Sect. A: Foundations.*, 2008, **64**, 112-122.
26. M. N. Blonsky, H. L. Zhuang, A. K. Singh and R. G. Hennig, Ab initio prediction of piezoelectricity in two-dimensional materials, *ACS Nano*, 2015, **9**, 9885-9891.
27. J. Zhao, H. Ge, Y. Wu, W. Xu, K. Xu, J. Ma, Q. Yang, C. Yue and X. Lei, Crystal rigidifying strategy toward hybrid cadmium halide to achieve highly efficient and narrowband blue light emission, *Mater. Today Chem.*, 2022, **24**, 100766.
28. R. Shannon, Revised effective ionic radii and systematic studies of interatomic distances in halides and chalcogenides, *Acta Crystallogr., Sect. A: Foundations*, 1976, **32**, 751-767.
29. W. Baur, The geometry of polyhedral distortions. Predictive relationships for the phosphate group, *Acta cryst. B*, 1974, **30**, 1195-1215.
30. M. S. Lassoued, M. S. M. Abdelbaky, W. Ben Soltan, A. Lassoued, S. Ammar, A. Gadri, A. Ben Salah and S. García-Granda, Structure characterization, photoluminescence and dielectric properties of a new hybrid compound containing chlorate anions of zincate (ii), *J. Mol. Struct.*, 2018, **1158**, 221-228.
31. M. Li and Z. Xia, Recent progress of zero-dimensional luminescent metal halides, *Chem. Soc. Rev.*, 2021, **50**, 2626-2662.
32. K. Karoui, A new hybrid layered perovskite $[CH_3–C_6H_4–NH_3]_2ZnBr_4$: Synthesis, crystal structure, optical and electrical properties, *J. Mol. Struct.*, 2020, **1203**, 127430.
33. S. Chkoundali, F. Hlel and H. Khemekhem, Synthesis, crystal structure, thermal and dielectric properties of tetrapropylammonium tetrabromozincate $[N(C_3H_7)_4]_2[ZnBr_4]$ compound, *Appl. Phys. A*, 2016, **122**, 1066.
34. H. Lin, C. Zhou, J. Neu, Y. Zhou, D. Han, S. Chen, M. Worku, M. Chaaban, S. Lee, E. Berkwits, T. Siegrist, M. Du and B. Ma, Bulk assembly of corrugated 1D metal halides with broadband yellow emission, *Adv. Optical Mater.*, 2019, **7**, 1801474.
35. K. Robinson, G. V. Gibbs and P. H. Ribbe, Quadratic elongation: A quantitative measure of distortion in coordination polyhedra, *Science*, 1971, **172**, 567-570.
36. L. Mao, Y. Wu, C. C. Stoumpos, M. R. Wasielewski and M. G. Kanatzidis, White-light emission and structural distortion in new corrugated two-dimensional lead bromide perovskites, *J. Am. Chem. Soc.*, 2017, **139**, 5210-5215.
37. S. Lee, C. Zhou, J. Neu, D. Beery, A. Arcidiacono, M. Chaaban, H. Lin, A. Gaiser, B. Chen, T. E. Albrecht-Schmitt, T. Siegrist and

B. Ma, Bulk assemblies of lead bromide trimer clusters with geometry-dependent photophysical properties, *Chem. Mater.*, 2019, **32**, 374-380.

38. D. Chen, F. Dai, S. Hao, G. Zhou, Q. Liu, C. Wolverton, J. Zhao and Z. Xia, Crystal structure and luminescence properties of lead-free metal halides $(C_6H_5CH_2NH_3)_3MBr_6$ (M = Bi and Sb), *J. Mater. Chem. C*, 2020, **8**, 7322-7329.
39. Y. Sui, W. Chen, S. Ouyang, W. Wang, G. Zhang and D. Liu, A semiconducting organic–inorganic hybrid metal halide with switchable dielectric and high phase transition temperature, *J. Phys. Chem. C*, 2019, **123**, 9364-9370.
40. T. Leijtens, R. Prasanna, A. Gold-Parker, M. F. Toney and M. D. McGehee, Mechanism of tin oxidation and stabilization by lead substitution in tin halide perovskites, *ACS Energy Lett.*, 2017, **2**, 2159-2165.
41. J. P. Perdew and M. Levy, Physical content of the exact kohn-sham orbital energies: Band gaps and derivative discontinuities, *Phys. Rev. Lett.*, 1983, **51**, 1884-1887.
42. E. R. Dohner, A. Jaffe, L. R. Bradshaw and H. I. Karunadasa, Intrinsic white-light emission from layered hybrid perovskites, *J. Am. Chem. Soc.*, 2014, **136**, 13154-13157.
43. C. Sun, Q. Zhong, X. Zhang, P. Xiao, Y. Cheng, Y. Gao, G. Liu and X. Lei, A zero-dimensional hybrid cadmium perovskite with highly efficient orange-red light emission, *Inorg. Chem.*, 2021, **60**, 18879-18888.
44. C. Zhou, H. Lin, J. Neu, Y. Zhou, M. Chaaban, S. Lee, M. Worku, B. Chen, R. Clark, W. Cheng, J. Guan, P. Djurovich, D. Zhang, X. Lü, J. Bullock, C. Pak, M. Shatruk, M. Du, T. Siegrist and B. Ma, Green emitting single-crystalline bulk assembly of metal halide clusters with near-unity photoluminescence quantum efficiency, *ACS Energy Lett.*, 2019, **4**, 1579-1583.